International Journal for Numerical Methods in Engineering

WILEY

RESEARCH ARTICLE

Spline-Based Framework for Microscopic Contact Zone Modeling in Lubricated Orthogonal Cutting

Jaewook Lee[1] | Jannis Saelzer[2] | Jacques Zwar[1] | Florian Zwicke[1] | Felipe Gonzalez[3] | Thomas Spenke[3] | Norbert Hosters[3] | Gero Polus[2] | Andreas Zabel[2] | Stefanie Elgeti[1,3]

[1]Institute of Lightweight Design and Structural Biomechanics, TU Wien, Vienna, Austria | [2]Institute of Machining Technology, TU Dortmund, Dortmund, Germany | [3]Chair for Computational Analysis of Technical Systems, RWTH Aachen, Aachen, Germany

Correspondence: Jaewook Lee (jaewook.lee@tuwien.ac.at)

Received: 28 September 2024 | **Revised:** 4 June 2025 | **Accepted:** 2 July 2025

Funding: This work was supported by the Deutsche Forschungsgemeinschaft (Grant No. 439919057 and 523163077).

Keywords: fluid-structure-contact interaction | microscopic contact | orthogonal cutting | spline

ABSTRACT

Accurately predicting the coefficient of friction between tool, chip, and workpiece during machining is essential for a reliable and cost-effective process. In this context, current numerical methods are often based on homogenized approaches with friction models that use constant friction coefficients; thus, failing to capture local effects. In addition, often neither the effect of lubricants nor the local tool and chip topographies is accounted for. Towards improving the state of the art in both respects, in this paper, we present a micro-scale friction model that can be coupled with a meso-scale chip formation model. The micro model determines a local friction coefficient based on local temperature, contact pressure, cutting speed, and lubricant wetting. It also incorporates the experimentally determined tool and chip topography. A key assumption of the model is that the main contribution to the friction coefficient is the interlocking of local roughness peaks. Our numerical implementation uses a combination of isogeometric analysis (IGA) for the chip and finite elements with spline-based boundaries for the fluid. This approach ensures a smooth, conformal interface between the cooling fluid and the chip, allowing for direct spatial coupling. Temporally, a Robin–Neumann coupling is used, which is critical for handling fully enclosed fluid pockets. The direct contact between the tool and the chip is modeled using a mortar knot-to-surface approach. To ensure computational affordability in this multi-query FE^2 scenario, a surrogate model for the micro-scale model is created using Gaussian process regression.

1 | Introduction

In machining, the friction between the tool and chip, as well as the tool and workpiece, significantly influences the manufacturing process. On the one hand, the resulting tool wear has an impact on process reliability and production costs [1]. On the other hand, the chip-surface integrity has a decisive influence on the application properties of the manufactured components [2]. The tribological loads have a significant influence on both of these effects during the manufacturing process. Accordingly, the tribological boundary conditions of the machining process must be designed to minimize loads in the critical contact areas. To this end, an effective solution is the application of cooling lubricants. When used properly, these can significantly reduce the thermo-mechanical load collectives on the tool and chip [3, 4]. However, the use of cooling lubricants also has disadvantages, such as high production costs, as well as environmental and health hazards [5, 6]. Accordingly, production engineering

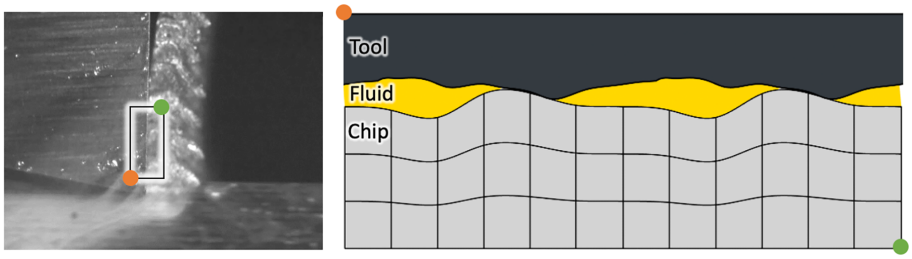

FIGURE 1 | Depiction of the secondary shear-zone in orthogonal cutting and the corresponding domain in the computational model. Orange and green dots are references for orientation.

research focuses on developing methods to minimize the use of cooling lubricants while maximizing their effectiveness. Achieving this requires comprehensive studies of machining processes, such as analyzing the impact of various cooling lubricants or tool surface topographies [7].

Numerical simulations have become an essential tool to gain a deeper understanding of the effects of cooling lubricants under specific processing conditions, offering insights into areas inaccessible to experimental observation. Depending on the scenario, different discretization methods are employed. In general, mesh-based approaches outperform particle-based methods regarding numerical efficiency and accuracy. In Reference [8], the impact of nanoparticle cooling is analyzed by predicting an accumulated heat transfer coefficient using a Lagrangian Discrete Phase Model (DPM), which is then integrated into a finite element-based chip formation simulation. By contrast, [9] investigates cryogenic Minimum Quantity Lubrication (MQL) during high-speed milling within a finite element context. Purely dry contact with varying cooling geometries is the focus of [10]. A finite difference method for analyzing the thermal behavior of tools during orthogonal cutting is presented in Reference [11], while [12] explores local contact conditions. Mesh-free methods, on the other hand, excel in handling topological changes. The focus of [13] is a Smoothed Particle Hydrodynamics (SPH) simulation of orthogonal metal cutting, emphasizing dynamic refinement for chip formation simulation and analysis. Similarly, SPH is employed in both [14] and [15]. In Reference [16], the Finite Pointset Method (FPM) is utilized to simulate orthogonal metal cutting, incorporating fluid-structure interaction (FSI) to account for cooling effects.

As established, numerical chip formation models are not only valuable tools for developing machining processes but are also frequently studied and refined in the literature. However, state-of-the-art models still face significant limitations, particularly in capturing the full complexity of the chip formation process. Accurately modeling phenomena such as the lubricating effects of cooling lubricants or microscopic adjustments to tool topography remains challenging. The primary issue lies in the friction models commonly used, as described in References [17, 18]. These friction models are often based on either the Coulomb model or Zorev's hybrid model [19], neither of which adequately account for the complex factors affecting friction in the chip formation zone, especially when constant model coefficients are employed [20, 21]. While empirical models, such as those presented in Reference [22], attempt to incorporate the effects of cooling lubricants or specific tool surface characteristics, they are difficult to calibrate and only valid under specific boundary conditions.

Therefore, the objective of this paper is to present a micro-scale friction model that can be integrated into a multi-scale framework for simulating chip formation, integrating both meso-scale and micro-scale simulations. At the meso-scale, any simulation model that can predict chip formation with an adjustable friction model can be used. The friction coefficients are then no longer constant, but are determined via a Python interface that links to the micro-scale model, which is the primary focus of this paper (cf. Figure 1). Within an FE^2 framework, the micro-scale model is evaluated at each Gauss point. The meso-scale model provides localized values for contact pressure, velocity, and temperature, while the micro-scale model determines corresponding friction coefficients.

Based on the assumption that the main contribution to the friction coefficient is the interlocking of local roughness peaks, the micro-scale model performs a high-resolution fluid-structure-contact interaction simulation involving the tool, modeled as a rigid body, the lubricating fluid, treated as an incompressible Newtonian fluid, and the chip, represented using the Johnson–Cook plasticity model. Fluid-structure-contact interaction (FSCI) forms the foundational basis for modeling tribological phenomena, particularly where lubrication and interface deformation are involved. The handling of such coupled problems remains an active area of research, especially in the finite element context, due to its inherent complexity and relevance in scientific and engineering applications [23]. Within monolithic frameworks, Burman et al. proposed Nitsche-based coupling schemes using a fully Eulerian approach [24–27] also employed Nitsche-type formulations, discretizing fluid domains via the CutFEM method, while [28] developed a unified-field fictitious domain method. In contrast, partitioned strategies have also been explored: [29] introduced a fully Eulerian variational framework for multiphase FSCI, and [30] employed a boundary-conforming space-time formulation [31] addressed FSCI using a fictitious domain approach with penalization. Notably, porous medium formulations have been adopted to model mechanically consistent transitions in fluid-structure and structure-structure interactions [24–26, 32], with Ager et al. [26] specifically addressing rough surface contact. It is known that the friction in the chip formation zone results from a superposition of different mechanisms of action. The effects in the sticking zone between the chip and rake face are determined by material adhesion and mechanical interlocking [33], although relatively little is known about the extent to which each of the mechanisms has an effect. The

study by Gregorio et al. suggests that for most metals (with the exception of titanium, which has an high affinity for reaction), a significant proportion of the frictional load can be attributed to mechanical interlocking [34], which is why this is envisaged as the defining mechanism for static friction in this study. Key to this approach is the local roughness topography, which has been determined experimentally using confocal microscopy. For the numerical implementation, we employ a combination of isogeometric analysis (IGA) for the chip and finite elements with spline-based boundaries for the fluid. This approach ensures a smooth, conformal interface between the cooling fluid and the chip, allowing for a direct spatial coupling. Temporally, a Robin–Neumann coupling is used, which is crucial for handling completely enclosed fluid pockets. The direct contact between the tool and chip is modeled using a mortar knot-to-surface approach. To guarantee computational affordability in this multi-query scenario of FE^2, a surrogate model for the micro-scale model is created using Gaussian Process regression.

In the remainder of the paper, we first present the numerical framework, detailing the physical models, the high-fidelity numerical methods, and the surrogate model. Furthermore, the behavior of the framework is demonstrated via numerical experiments.

2 | Numerical Framework: Spline-Based Fluid-Structure-Contact Interaction

In this section, we present a spline-based fluid-structure-contact interaction model that is generally applicable, but for the purpose of this paper, has been applied as a micro-model for lubricated contact in orthogonal cutting. The section is organized according to the individual components of the framework: Structure, fluid, and the interaction thereof. For each problem, we present theoretical backgrounds and solution methods.

2.1 | Structural Problem

In the framework, the behavior of a structural body is expressed in terms of a displacement field. Based on a total Lagrangian viewpoint, the displacement field $\boldsymbol{u}$ is formulated with respect to a reference (undeformed) configuration Ω^s_{ref} and is governed by the equation of motion

$$\rho^s \frac{d^2\boldsymbol{u}}{dt^2} = \nabla_{ref} \cdot \boldsymbol{P} + \boldsymbol{b}^s \qquad \text{in} \quad \Omega^s_{ref} \tag{1}$$

where ρ^s, $\boldsymbol{b}^s$, $\boldsymbol{P}$ denote structural density, body force, and first Piola–Kirchhoff stress, respectively; ∇_{ref} implies the gradient with respect to the reference configuration. The stress here is a function of the deformation gradient, i.e., $\boldsymbol{P}(\boldsymbol{F})$, which represents a constitutive response. Additionally, the structural problem is subjected to initial conditions as well as Dirichlet and Neumann boundary conditions:

$$\boldsymbol{u}(t=0) = \boldsymbol{u}_0 \qquad \text{in} \quad \Omega^s_{ref} \tag{2}$$

$$\boldsymbol{u} = \boldsymbol{g}^s \qquad \text{on} \quad \Gamma^s_D \tag{3}$$

$$\boldsymbol{P}\boldsymbol{n}^s_{ref} = \boldsymbol{h}^s \qquad \text{on} \quad \Gamma^s_N \tag{4}$$

where Γ^s_D and Γ^s_N denote Dirichlet and Neumann part of the boundary; $\boldsymbol{g}^s$ and $\boldsymbol{h}^s$ are prescribed boundary displacement and traction, respectively; $\boldsymbol{n}^s_{ref}$ is the outward pointing unit normal vector in the reference configuration.

The structural problem is solved numerically using the MFEM library [35] with NURBS-based isogeometric analysis (IGA) [36] in space and a *generalized-α* time integration scheme [37].

There are two structures to consider in the micro model: The tool and the chip. While the tool is modeled as a rigid body, the chip is represented by a nonlinear plasticity model with Johnson–Cook hardening, which reads as follows:

$$\sigma_y = \left[A + B\left(\overline{\epsilon}^{pl}\right)^n\right]\left[1 + C ln\left(\frac{\dot{\overline{\epsilon}}^{pl}}{\dot{\epsilon}_0}\right)\right]\left(1 - \hat{\theta}^m\right) \tag{5}$$

with

$$\hat{\theta} \equiv \begin{cases} 0 & \text{for} \quad \theta \le \theta_{transition}, \\ (\theta - \theta_{transition})/(\theta_{melt} - \theta_{transition}) & \text{for} \quad \theta_{transition} \le \theta < \theta_{melt}, \\ 1 & \text{for} \quad \theta_{melt} \le \theta \end{cases} \tag{6}$$

where σ_y is the yield stress, $\overline{\epsilon}^{pl}$ is the equivalent plastic strain, $\dot{\overline{\epsilon}}^{pl}$ is the equivalent plastic strain rate, $\hat{\theta}$ is non-dimensional temperature. $A, B, n, m, \theta_{melt}$, and $\theta_{transition}$ denote material parameters. For plasticity, we follow J_2 flow theory at finite strains formulation presented in Reference [38]. Finally, thermal effects are considered adiabatic.

2.2 | Fluid Problem

The cooling lubricant in the micro model is represented using the incompressible Navier–Stokes equations, which describe the dynamics of a viscous fluid in terms of velocity $\boldsymbol{v}$ and pressure p:

$$\rho^f\left(\frac{\partial \boldsymbol{v}}{\partial t} + \boldsymbol{v} \cdot \nabla \boldsymbol{v}\right) - \nabla \cdot \boldsymbol{\sigma} = \rho^f \boldsymbol{b}^f \qquad \text{in} \quad \Omega^f \tag{7}$$

$$\nabla \cdot \boldsymbol{v} = 0 \qquad \text{in} \quad \Omega^f \tag{8}$$

where ρ^f is the fluid density and $\boldsymbol{b}^f$ the volume forces. We consider the cooling lubricant to be Newtonian, leading to a stress tensor $\boldsymbol{\sigma}$ defined as:

$$\boldsymbol{\sigma} = -p\boldsymbol{I} + \eta\left(\nabla \boldsymbol{v} + (\nabla \boldsymbol{v})^T\right) \tag{9}$$

where η is the dynamic viscosity. The fluid problem is also subjected to initial conditions as well as Dirichlet and Neumann, and Robin boundary conditions:

$$\boldsymbol{v}(t=0) = \boldsymbol{v}_0 \qquad \text{in} \quad \Omega^f \tag{10}$$

$$\boldsymbol{v} = \boldsymbol{g}^f \qquad \text{on} \quad \Gamma^f_D \tag{11}$$

$$\boldsymbol{\sigma}\boldsymbol{n}^f = \boldsymbol{h}^f \qquad \text{on} \quad \Gamma^f_N \tag{12}$$

$$\alpha^R \boldsymbol{v} + \boldsymbol{\sigma}\boldsymbol{n}^f = \boldsymbol{h}^f + \alpha^R \boldsymbol{g}^f \qquad \text{on} \quad \Gamma^f_R \tag{13}$$

where Γ^f_D, Γ^f_N, and Γ^f_R denote Dirichlet, Neumann, Robin part of the fluid boundary with prescribed velocity $\boldsymbol{g}^f$ and traction $\boldsymbol{h}^f$; α^R is the scalar weighting factor for Robin boundary condition.

The fluid problem is solved using stabilized finite elements in space [39] and an implicit Euler time integration scheme. Moreover, an arbitrary Lagrangian–Eulerian formulation is employed to accommodate a moving fluid domain, where the mesh is adapted using a linear elastic mesh-update method (EMUM) [40]. Moving boundaries are represented using NURBS, which enables the definition of displacements directly through the control points. Further information about the fluid solver can be found in References [41, 42].

2.3 | Interface Interactions

2.3.1 | Partitioned FSI Approach

As the fluid and structural domains share an interface, the solution fields become naturally dependent on each other and require coupling. In this work, we adopt a partitioned approach: Two individual solvers—one for each domain—are coupled through a coupling module. Where necessary, properties at the interface are exchanged iteratively to fulfill temporal and spatial coupling conditions.

To fulfill temporal coupling conditions at each time step, the solvers are strongly coupled through fixed-point iterations [43]. Starting with initial guesses on both sides, the following procedure is repeated until convergence: (1) given structural displacement at the interface, compute fluid load (kinematic continuity); (2) given the fluid load at the interface, compute structural displacement (dynamic continuity). This is often referred to as Dirichlet–Neumann coupling [44]. Note that a Robin–Neumann coupling is used to circumvent the so-called incompressibility dilemma of classical Dirichlet–Neumann schemes for fully-enclosed incompressible fluids [45, 46]. Accordingly, in step (1), a Robin boundary condition is imposed on the flow problem, formed from the current deformation state and the previous interface tractions, as proposed by [46].

The spatial coupling regards the transfer of the related properties that become boundary conditions for the other domain. This is especially relevant when different discretization techniques are employed, requiring a conservative projection method. With the finite interpolation method [44, 47], arbitrary data associated at specific points of the interface can be projected to the destination domain by multiplying their corresponding basis functions. Within this work, we apply the spline-based formulation presented in Reference [44].

2.3.2 | Contact Enforcement

The interactions between structural bodies are considered a contact problem. Since two bodies cannot physically overlap and the location is unknown a priori, this becomes a nonlinear optimization problem to solve at the interface level [48]. Throughout this work, we adopt the mortar knot-to-surface formulation [49, 50]. Enforcing the impenetrability condition starts by defining a normal gap g_n between a point $\boldsymbol{x}_q$ on contact boundary Γ_C^s and its nearest projection point $\boldsymbol{x}_p$ on the opposing contact boundary Γ_{CO}^s:

$$g_n = (\boldsymbol{x}_p - \boldsymbol{x}_q) \cdot \boldsymbol{n}_p \tag{14}$$

where $\boldsymbol{n}_p$ denotes the outward pointing normal at the projection point. Following the mortar knot-to-surface formulation [49, 50], we then compute the contact pressure p_{na} using weighted average of the normal gaps g_{na}, associated to the individual control points:

$$g_{na} = \frac{\int_{\Gamma_C^s} N \; g_n \; \mathrm{d}\Gamma}{\int_{\Gamma_C^s} N \; \mathrm{d}\Gamma} \tag{15}$$

$$p_{na} = \epsilon g_{na} \tag{16}$$

where N denotes the basis function for a given control point and ϵ is a penalty factor. It is important to note that for splines of higher degrees than one, finding the nearest projection point becomes an optimization problem. Within this work, we minimize a squared distance function $\boldsymbol{J}_d(\xi) = (\boldsymbol{x}_q - \boldsymbol{x}_p(\xi))^2$ to determine the parametric position ξ of the closest projection point and employ the Newton method, Levenberg–Marquardt algorithm [51], and sequential quadratic programming [52] to ensure convergence.

3 | Micro-Model Towards Friction Modeling

The micro model is intended to provide insight into the complex tribological interactions in the secondary shear zone (see Figure 1). In particular, we aim to develop a robust and extensible setup that can incorporate all factors influencing friction coefficients and behavior referenced in characterization experiments [22, 53]: Tool topography, lubricants, normal pressure, and relative tangential velocity. As a result, we can use the model to characterize friction on any topography and boundary conditions of interest, e.g., to improve the simulation of chip formation used for tool development.

Using the proposed spline-based fluid-structure-contact interaction framework detailed in Section 2, we have developed a model that represents the contact zone at the microscopic level and can incorporate the above factors. In the remainder of this paper, we investigate its capability to characterize friction.

3.1 | High-Fidelity Model

The starting point of the numerical model is the geometric modeling of the domain, incorporating the microscopic tool topography into the analysis. Based on actual measurements of the surface topography of both the tool and chip, we create a spline representation using a spline fitting technique [54]. The fitted surface is then extruded to form a volumetric structural domain suitable for analysis using IGA.

The two structural domains, Ω_T and Ω_W, correspond to the tool and chip, respectively. The tool is treated as a rigid body, while the chip is modeled as a Johnson–Cook material [55]. Within this work, we adopt the material parameters presented in Reference [53]. The fluid within the domain Ω_F is incompressible. At the chip boundary, Γ_W, the chip can interact with both the fluid and the tool. It is important to note that this model permits only a single type of interaction at each physical location of the boundary at any given time. However, due to the high continuity of the B-spline basis function, it is possible for loading from both sources to manifest in the same location.

A partitioned approach is used to couple the fluid and structural domains. For spatial coupling, we utilize a spline-based finite interpolation method [44], which leverages identical spline representations at the interface. The Robin–Neumann temporal coupling scheme mitigates the incompressibility dilemma [46], arising from the fluid domain being surrounded by the structural domain. Domain deformations caused by the moving fluid interface are accounted for using EMUM [40].

To account for pressure and relative velocity, we apply normal pressure to the vertical degrees of freedom (y) and prescribe horizontal (x) displacement at Γ_B. On $\Gamma_{periodic}$, a periodic boundary condition is implemented—for both fluid and structural domains—to reflect that the model represents a portion of a larger statistically repeating domain. Lastly, we incorporate a temperature introduced as an initial condition to characterize the material state.

With these conditions established, the computation begins by moving the chip at a specified relative velocity while applying pressure on the bottom of the chip domain and initial fluid loads. The structural solver produces a displacement field that satisfies the contact condition, which is then relayed to the fluid solver. Based on the interface displacement, the fluid solver deforms the domain and computes the resulting loads at the interface, which are passed back to the structural solver. This process iterates at each time step until convergence is achieved for both solvers.

3.2 | Reduced Model

The objective of the high-fidelity model is to predict the friction behavior based on the microscopic topography, material state, and boundary conditions. In particular, the coefficients of friction under certain boundary conditions—such as pressure, temperature, and relative velocity—can be used in chip formation simulations to provide valuable insight into cutting operations. Within our micro-model, the friction coefficient μ is calculated as the ratio of the vertical T_x and horizontal T_y components of the integrated applied traction vector $\boldsymbol{T}$ along the interface:

$$\mu = \frac{\int_{\Gamma_W} T_x \, \mathrm{d}\Gamma}{\int_{\Gamma_W} T_y \, \mathrm{d}\Gamma} \tag{17}$$

For dynamic simulations, a time-averaged value μ within given time steps is used. However, calculating these coefficients locally for every element of the meso simulation using a high-fidelity model is computationally too demanding. Therefore, a reduced model is needed to efficiently provide this information with significantly less computational effort.

In this work, we use Gaussian process regression [56] to develop a reduced model for the characterized friction coefficient. This model approximates the friction coefficient as a function of pressure, relative velocity, and temperature. We employ the implementation provided in *scikit-learn* [57] package with radial basis function kernel. For the training set, 900 data points are prepared, and hyperparameters of the kernel are also optimized during the training.

4 | Numerical Examples

In this section, we examine the model's behavior with respect to application-related boundary conditions. The main goal of the micro-model is to provide a flexible friction modeling framework that serves as the basis for further chip formation simulation and tool design. Given pressure, relative velocity, and initial temperature, the model computes the chip's deformation and applied forces, which can then be used to determine friction coefficients (see Equation (17)).

We utilize the geometry created based on surface topography measurement (see Figure 2). Then, we define the range of required boundary conditions based on the process conditions reported in previous experiments, see [22, 53]. The prescribed pressure and relative velocity at Γ_B range from 300 MPa to 1,300 MPa and 22.5 m/min to 200 m/min, respectively. The initial temperature of the chip ranges from 25°C to 900°C. From these ranges, we uniformly sample values for characterization computations.

The penalty factor for computing contact pressure (see Equation (16)) is 2×10^{18}. The geometry close to the contact region is uniformly refined until the friction coefficient computation converges with less than 0.7%. As discussed at the end of Section 3.1, periodic boundary conditions are applied so only a single interval represents our structural domain in the model problem. We employed Newton's method with a line search technique—specifically, the Quadratic Variation of the Norm of the Residual Line Search [58]—to solve the nonlinear system of equations, and used a direct solver for the associated linear systems. For visualization purposes, Figures 3 and 4 show a section that is two intervals long to help illustrate the structural deformation at a given time step. The structural material parameters used in the computations are shown in Table 1 and fluid material parameters are shown in Table 2.

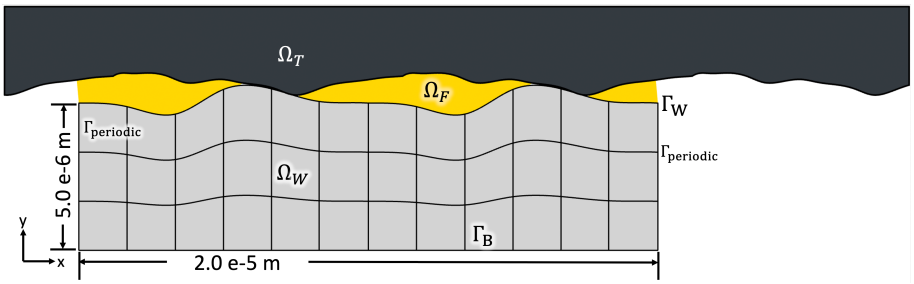

FIGURE 2 | Computational domain of the high-fidelity model.

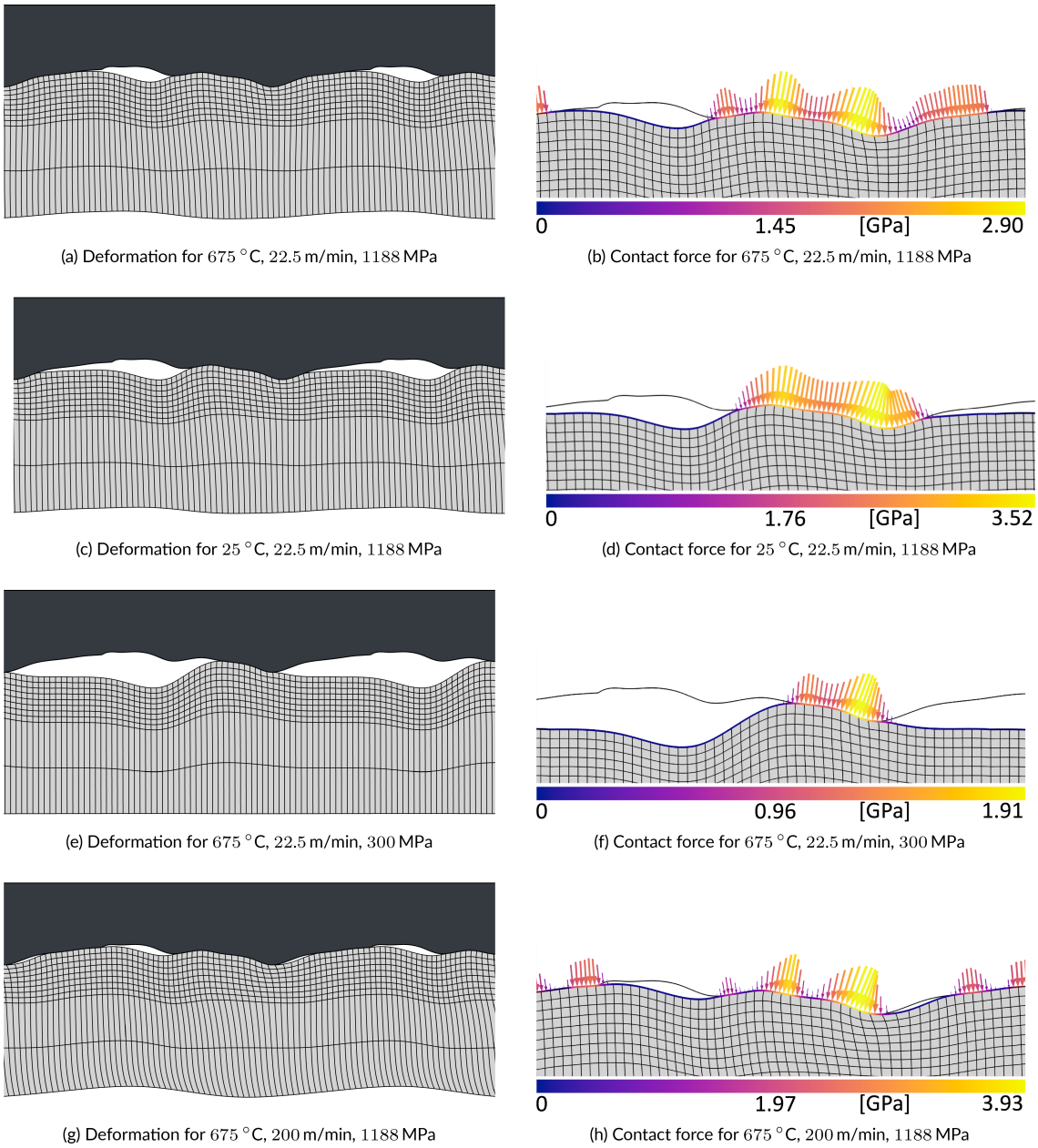

(a) Deformation for 675 °C, 22.5 m/min, 1188 MPa

(b) Contact force for 675 °C, 22.5 m/min, 1188 MPa

(c) Deformation for 25 °C, 22.5 m/min, 1188 MPa

(d) Contact force for 25 °C, 22.5 m/min, 1188 MPa

(e) Deformation for 675 °C, 22.5 m/min, 300 MPa

(f) Contact force for 675 °C, 22.5 m/min, 300 MPa

(g) Deformation for 675 °C, 200 m/min, 1188 MPa

(h) Contact force for 675 °C, 200 m/min, 1188 MPa

FIGURE 3 | Results of the high-fidelity model computation with dry contact for various boundary conditions after a complete time step of 2.5×10^{-7} s, showing both the deformation state of the chip as well as the associated contact force. The left column shows two intervals of the deformed domain, spanning a total width of 2×10^{-5} m, while the right column presents a magnified view of approximately one such interval, focusing on the geometric peaks of the tool. The local normal contact force on the tool-chip interface achieves a maximum value of 3.93 GPa.

The resulting deformed states of the chips under various boundary conditions for dry contact are shown in Figure 3. Due to the prescribed pressure, the chip deforms and closes the void between itself and the tool. This also causes the bottom of the chip to deform, given a sufficient amount of pressure proportional to the size of the void. With increasing temperature (Figure 3a,c), the deformation becomes more significant. A similar trend can be observed with increasing boundary pressure (see Figure 3a,e).

Most notably, the force distribution changes considerably with increased relative tangential velocity (Figure 3b,h). At higher velocities, the contact zone between chip and tool becomes less concentrated, resulting in an uneven distribution of the contact forces with local peaks. These high-pressure zones are located at geometric spikes of the chip, resulting in steep normal vectors at the regions of contact with high magnitudes of the horizontal forces. Accordingly, these regions contribute more importantly to the overall resistance of the chip movement, resulting in higher friction coefficients.

Unlike dry contact, lubricated contact, as shown in Figure 4, under the same boundary conditions, exhibits more evenly distributed forces on the chip at the boundary Γ_W. Force peaks are only observed at the initial minimal gap that separates the tool and the chip, which consequently leads to a local deformation. The incompressibility of the fluid results in a more uniform force

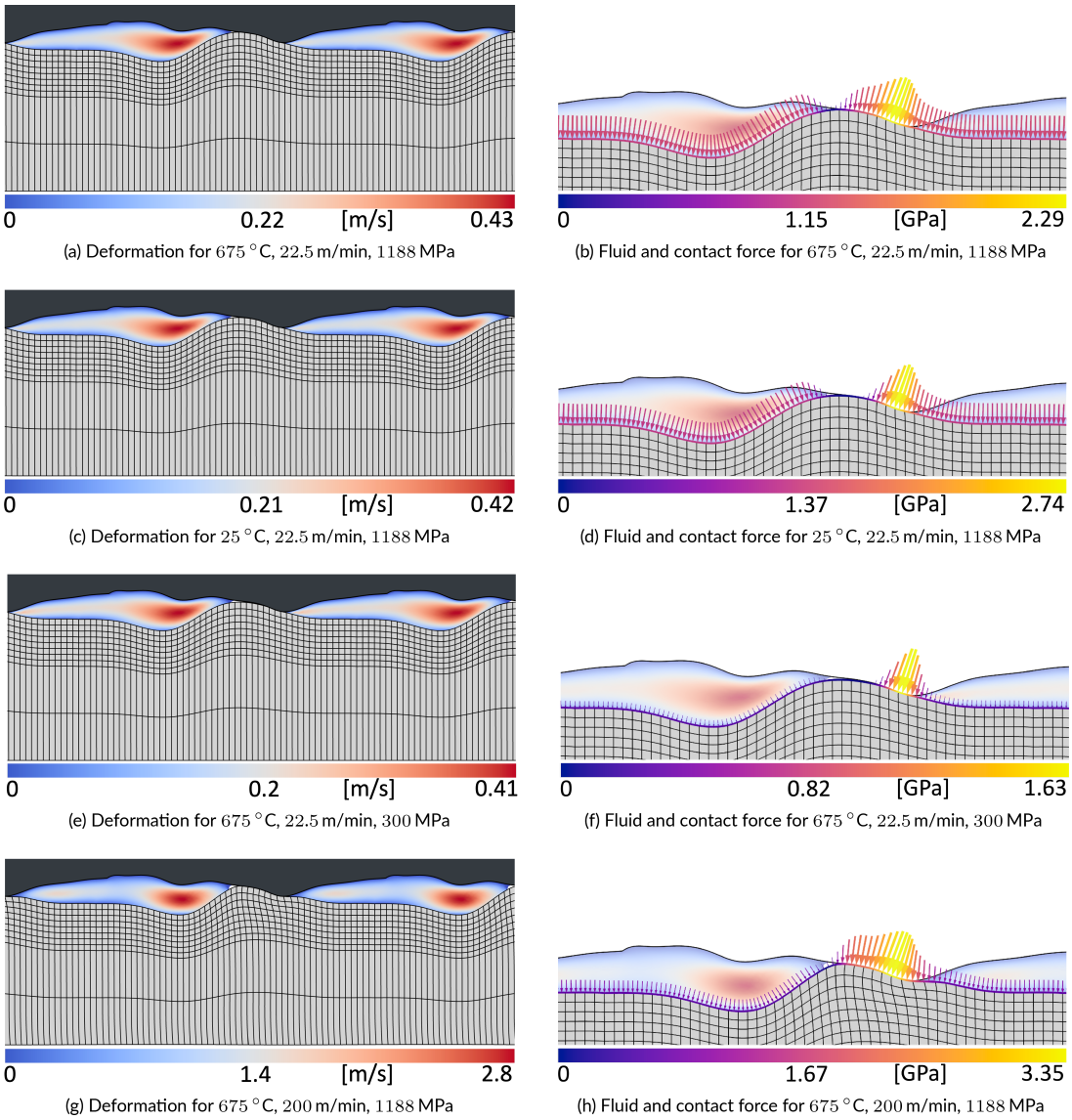

FIGURE 4 | Results of the high-fidelity model computation with lubricated contact for various boundary conditions after 2.5×10^{-7} s. The fluid is encapsulated in the gaps between the chip and tool; the colors depict the velocity magnitude of the fluid. Viewpoints are consistent with those in Figure 3. The local normal contact force on the tool achieves a maximum value of 3.35 GPa.

TABLE 1 | Material parameters for structure.

Structure parameters	Value
Density	$7,800$ kg m^{-3}
Young's Modulus	205 GPa
Poisson's Ratio	0.29
A	288 MPa
B	695 MPa
C	0.034
n	0.2835
m	1.3558
$\dot{\epsilon}_0$	0.004 S^{-1}
$\theta_{transition}$	20
θ_{melt}	1,500
Specific Heat Capacity	450 J kg^{-1} K^{-1}
Heat Fraction	0.9

TABLE 2 | Material parameters for incompressible fluid.

Fluid parameters	Value
Density	800 kg m^{-3}
Dynamic viscosity	0.032 kg m^{-1} s^{-1}

distribution in all areas that are touched by the fluid. Additionally, this incompressibility prevents further deformation of the chip, which can occur in dry contact due to the presence of voids instead of fluid. By increasing relative velocity, an increase in the force magnitude can be seen at the contact boundary. In some regions, the fluid force points in the same direction as the chip motion. Unless the chip has a flat surface, such an area can always be observed. This is an additional effect of the lubrication fluid, which now causes thrust and therefore reduces the coefficient of friction.

(a) Velocity magnitude (b) Pressure magnitude

FIGURE 5 | Fluid field under boundary conditions at 675°C, 22.5 m min^{-1} and 300 MPa after 2.5×10^{-7} s. The full domain is shown in Figure 4e.

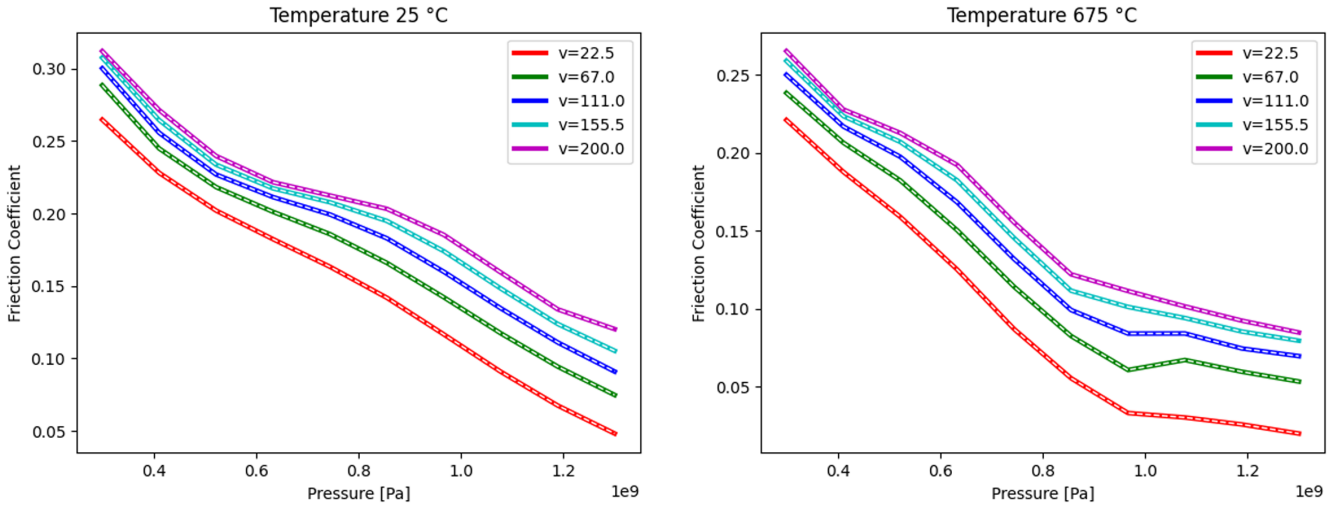

(a) Friction coefficient at 25 °C (b) Friction coefficient at 675 °C

FIGURE 6 | Friction coefficient (dry) from high-fidelity model and reconstruction with reduced model (white dashed line) at varying boundary conditions.

A detailed view of the internal flow field is shown in Figure 5. The magnitude of the velocity is within the order of the relative velocity between chip and tool, which is consistent with the mesh velocity boundary condition during FSI coupling. Furthermore, the velocity vector is aligned with the direction of chip motion. The pressure field shows a homogeneous profile. While the left side, where the chip is fed forward, causing a "squeezing" effect, shows a slightly higher pressure, the relative difference between the maximum and minimum value is 27%.

As briefly mentioned in Section 3.2, the friction coefficient in this work is computed as a ratio between the integrated force in the horizontal and vertical directions (see Equation (17)). Figure 6 shows the result of friction characterization without lubrication. We observe a general decrease in the friction coefficient with increasing pressure and increasing relative velocity. On the other hand, an increase in temperature results in a decrease in the friction coefficient.

Friction coefficients from the lubricated model, shown in Figure 7, share similar tendencies with the dry model. The friction coefficient decreases with increasing pressure, increasing relative velocity, and increasing temperature.

The corresponding reduced models are trained using the 900 sampled results for dry and lubricated contact. The trained models are tested with 200 randomly sampled datasets, which resulted in 1% (dry) and 1.8% (lubricated) mean relative error. The reconstructed data from the reduced models are shown as dashed lines in Figures 6 and 7, which agree well with the high-fidelity data. Training data reconstruction resulted in 2.3×10^{-5}% (dry) and 9.8×10^{-4}% (lubricated) mean relative error.

The trained reduced model's predictions, along with the 95% confidence intervals, are illustrated in Figures 8 and 9. They show the predicted mean values as a solid line, while the shaded regions represent the confidence intervals, indicating the uncertainty of the model's predictions. Since the training data is uniformly sampled, the uncertainties remain low within the data range. A slight increase in uncertainty is observed towards both ends of the interval, particularly for the dry model. As expected, the uncertainty grows more significantly outside the data range.

The computational cost of the high-fidelity model is measured and compared with the reduced model by evaluating their execution times on a single core of an AMD Ryzen 7 3700X processor. The average execution times for the high-fidelity dry and lubricated models are 1.3 h and 6.4 h, respectively. In contrast, the reduced model consistently completes in under 0.00015 s, offering speed-ups of 3.12×10^7 and 1.54×10^8, respectively. It is important to note that evaluating the reduced model requires a preliminary offline phase, which involves preparing the dataset and training the model. Running high-fidelity simulations for all sampling points—both dry and lubricated—required approximately 7,000 h of wall-clock time. With a high-fidelity dataset in place, training the reduced model took only 20 s. Potentially, active learning could reduce the cost of high-fidelity simulations by iteratively adding sampling points in high-uncertainty regions of the input space and retraining the model.

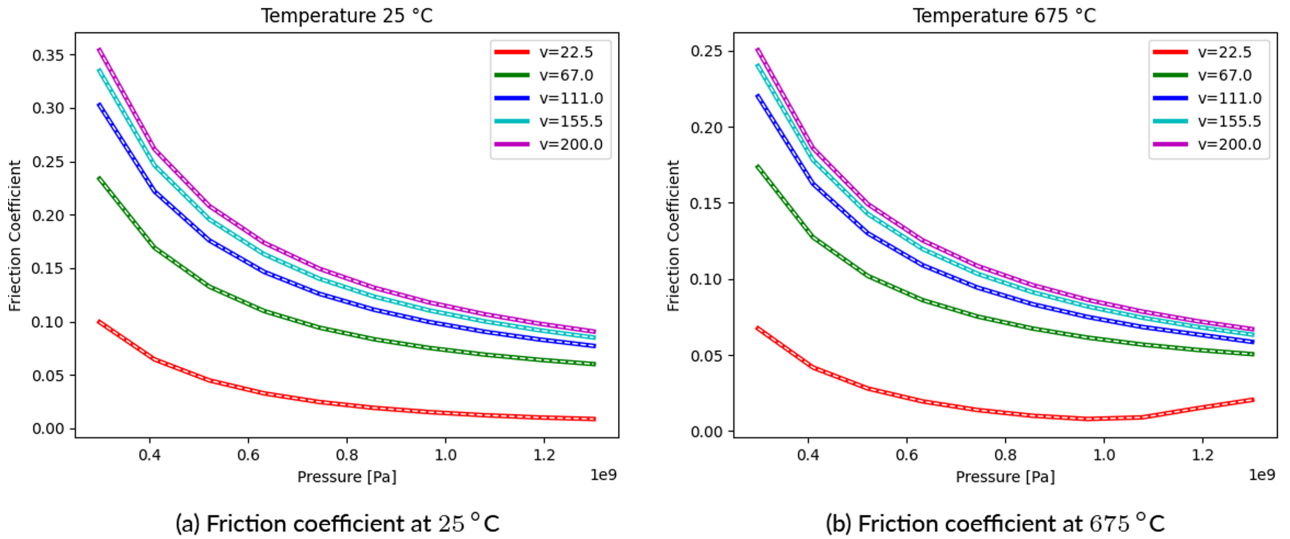

(a) Friction coefficient at 25 °C (b) Friction coefficient at 675 °C

FIGURE 7 | Friction coefficient (lubricated) from high-fidelity model and reconstruction with reduced model (white dashed line) at varying boundary conditions.

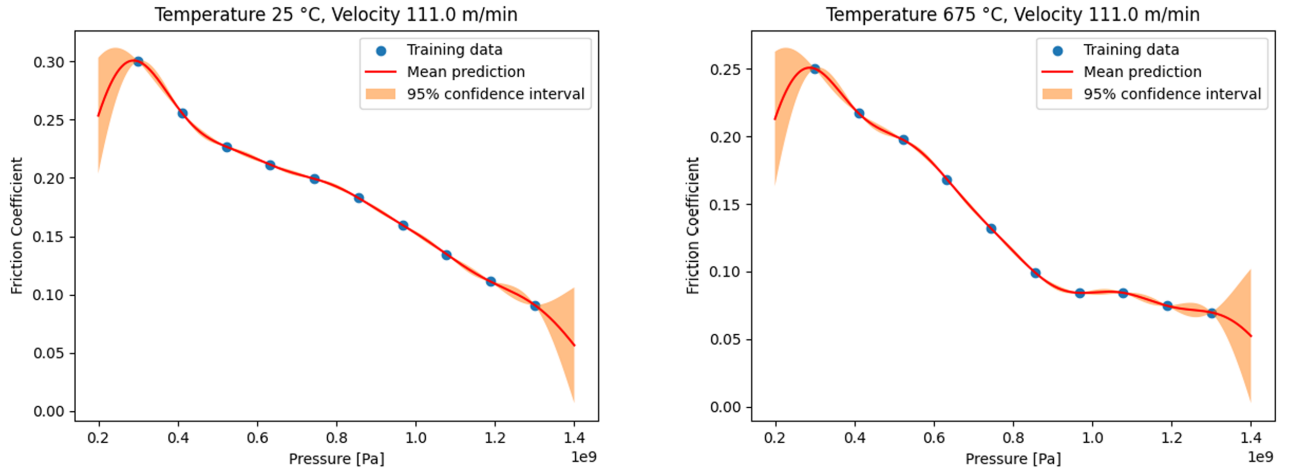

(a) Friction coefficient prediction at 25 °C (b) Friction coefficient prediction at 675 °C

FIGURE 8 | Friction coefficient predictions (dry) and their 95% confidence interval from reduced model at 111 m min^{-1}. The sample range includes regions that are not present in the training data.

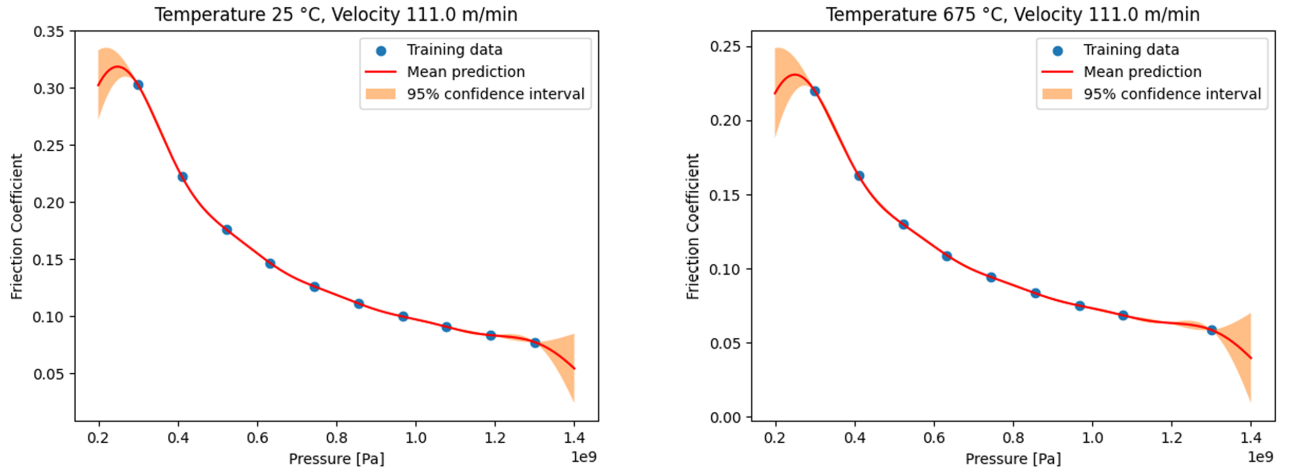

(a) Friction coefficient prediction at 25 °C (b) Friction coefficient prediction at 675 °C

FIGURE 9 | Friction coefficient predictions (lubricated) and their 95% confidence interval from reduced model at 111 m min^{-1}. The sample range includes regions that are not present in the training data.

5 | Discussion and Outlook

In this work, we have investigated the applicability of a high-fidelity fluid-structure-contact interaction model and a corresponding reduced model for friction modeling in chip formation simulations. The numerical experiments show that, in contrast to existing models, our micro-model can (1) provide a localized friction coefficient based on boundary conditions for temperature, contact pressure, and relative velocity; (2) incorporate the effects of lubricating fluids; and (3) account for an experimentally determined characteristic tool and chip topography. Numerically, a key feature of the model is the use of spline-based methods, which accurately represent the measured topographies, provide continuous and uniquely defined normal vectors for the contact formulation, and also exhibit higher accuracy per degree of freedom compared to standard finite elements. Another important aspect of the presented method is the temporal Robin–Neumann coupling during the partitioned FSI approach, which is the only way to handle the fully enclosed fluid pockets, which are inevitable in this modeling approach. Overall, a fully functional fluid-structure-contact interaction framework has been developed that provides a number of features required by the micro-model. Further, the framework is fully modular, facilitating process-specific extensions if necessary. Furthermore, a reduced model based on Gaussian process regression was presented. It provides accurate results at a significantly lower computational cost, allowing multi-scale coupled simulation in a reasonable time. The reduced model is entirely non-intrusive and can be continuously extended as novel data points become available.

Using both the high-fidelity and the reduced model, we investigate the resulting friction coefficients for varying temperature, relative velocity, and contact pressure over a wide range of experimentally deducted process-relevant values. For the dry model, it is observed that an increase in temperature leads to a decrease in the coefficient of friction. This is due to the temperature dependence of the plasticity model, where a higher temperature results in higher deformations and thus a larger contact area between the tool and chip. The effect of pressure is similar to that of temperature, as an increase in pressure results in a bigger contact area. Combined with the more uniform force distribution, the horizontal components on opposite sides of the local peaks counteract one another, leading to a reduction in the overall friction coefficient. The relative velocity, however, has the opposite effect. As the velocity increases, the distribution of contact zones becomes sparser, leading to more irregular and locally concentrated forces at the chip interface, particularly around the spikes of the microscopic surface geometry, where steeper slopes generate greater ratios between the horizontal and vertical force components. This ultimately results in higher coefficients of friction.

It is important to note that to ensure higher accuracy and lower uncertainty in the reduced model, training data should include samples that cover the entire expected range of the boundary conditions, i.e., input state variables that originate from the meso model, during the chip formation simulation process. In cases where runtime query is out of the bounds of the training data, i.e., if the model needs to extrapolate, it can be trained iteratively by adding samples in areas where uncertainties are high, continuing this process until the desired accuracy is achieved.

The lubricated contact model generally shows a coefficient of friction behavior similar to the dry model. An important difference, however, is that the deformation pattern of the chip is now less localized. This is due to the fact that the forces applied at the interface are more homogeneous, and the contact area is limited to areas without lubricant. In fact, it is these areas that contribute most to the coefficient of friction.

If one compares the described behavior of the micro model with experimentally observed tendencies, e.g., in Reference [59], one notices discrepancies with respect to the influence of velocity and contact pressure: In the real system, the coefficient of friction increases with normal contact pressure until it levels off at some point. Furthermore, as the relative velocity increases, the coefficient of friction decreases. One can conclude that neither effects is dominated by the mechanical interaction between the rough surfaces, as was our initial assumption.

In future work, the presented modular framework may therefore be extended to include additional tribological mechanisms. One example is an adhesion model, which can help to capture interatomic forces. The influence of thermal effects can be handled more accurately by considering a temperature field for each domain rather than a single adiabatic temperature field for workpieces. This can also allow for heat transfer between domains, both fluid-structure and structure-structure interactions, incorporating cooling/heating effects into the model. In addition, the fluid could be modeled as a shear-thinning fluid to more accurately capture its behavior. Boundary conditions, e.g., pressure-based resistance, for the fluid can be further explored to accommodate domains with open ends. The magnitude may be validated through experimental studies. Finally, since the secondary shear zone has already undergone plastic deformation, information about the accumulated plastic strain can be used as an initial condition in the model. On the numerical side, the spatial coupling could benefit from the adoption of the NURBS-enhanced finite-element method [60], which could further improve the accuracy of the fluid simulation. This could render the implementation of more advanced mesh refinement methods possible, resulting in a higher accuracy of the high-fidelity model.

Subsequently, the micro-model will be integrated into meso-scale chip formation simulations. Our goal is to adopt this multi-scale framework to enhance the tool design process, enabling predictions of tool, chip, and product behavior in relation to the previously mentioned influencing factors. The framework's applicability will be assessed through experimental validation.

Acknowledgments

Funded by the Deutsche Forschungsgemeinschaft (DFG, German Research Foundation). Gefördert durch die Deutsche Forschungsgemeinschaft (DFG)—Projektnummer 439919057, 523163077.

Conflicts of Interest

The authors declare no conflicts of interest.

Data Availability Statement

The data that support the findings of this study are available from the corresponding author upon reasonable request.

References

1. P. Mativenga, J. Schoop, I. Jawahir, et al., "Engi . . . mance and Customized Applications: A Review," *CIRP Journal of Manufacturing Science and Technology* 52 (2024): 212–228, https://doi.org/10.1016/j.cirpj.2024.06.001.

2. A. Malakizadi, R. Bertolini, F. Ducobu, Z. Kilic, M. C. Magnanini, and A. Shokrani, "Recent Advances in Modelling and Simulation of Surface Integrity in Machining-A Review," *Procedia CIRP* 115 (2022): 232–240. 10th CIRP Global Web Conference-Material Aspects of Manufacturing Processes, https://doi.org/10.1016/j.procir.2022.10.079.

3. F. Pape, G. Poll, L. Ellersiek, B. Denkena, and H. Liu, "Tribological Effects of Metalworking Fluids in Cutting Processes," *Lubricants* 11, no. 5 (2023): 224, https://doi.org/10.3390/lubricants11050224.

4. R. Teti, D. D'Addona, and T. Segreto, "Microbial-Based Cutting Fluids as Bio-Integration Manufacturing Solution for Green and Sustainable Machining," *CIRP Journal of Manufacturing Science and Technology* 32 (2021): 16–25, https://doi.org/10.1016/j.cirpj.2020.09.016.

5. M. Chen, R. Peng, L. Zhao, R. Chen, and Y. Luo, "Effects of Minimum Quantity Lubrication Strategy With Internal Cooling Tool on Machining Performance in Turning of Nickel-Based Superalloy GH4169," *International Journal of Advanced Manufacturing Technology* 118, no. 11–12 (2022): 3673–3689, https://doi.org/10.1007/s00170-021-08194-w.

6. T. He, N. Liu, H. Xia, et al., "Progress and Trend of Minimum Quantity Lubrication (Mql): A Comprehensive Review," *Journal of Cleaner Production* 386 (2023): 135809, https://doi.org/10.1016/j.jclepro.2022.135809.

7. I. Jawahir, H. Attia, D. Biermann, et al., "Cryogenic Manufacturing Processes," *CIRP Annals* 65, no. 2 (2016): 713–736, https://doi.org/10.1016/j.cirp.2016.06.007.

8. I. Nouzil, A. Eltaggaz, I. Deiab, and S. Pervaiz, "Numerical Cfd-Fem Model for Machining Titanium Ti-6al-4v With Nano Minimum Quantity Lubrication: A Step Towards Digital Twin," *Journal of Materials Processing Technology* 312 (2023): 117867, https://doi.org/10.1016/j.jmatprotec.2023.117867.

9. H.-P. Zhang, Q.-Y. Zhang, Y. Ren, T. Shay, and G.-L. Liu, "Simulation and Experiments on Cutting Forces and Cutting Temperature in High Speed Milling of 300m Steel Under Cmql and Dry Conditions," *International Journal of Precision Engineering and Manufacturing* 19 (2018): 1245–1251.

10. S. Saketi, J. Östby, and M. Olsson, "Influence of Tool Surface Topography on the Material Transfer Tendency and Tool Wear in the Turning of 316l Stainless Steel," *Wear* 368-369 (2016): 239–252, https://doi.org/10.1016/j.wear.2016.09.023.

11. W. Grzesik, M. Bartoszuk, and P. Nieslony, "Finite Difference Analysis of the Thermal Behaviour of Coated Tools in Orthogonal Cutting of Steels," *International Journal of Machine Tools & Manufacture* 44, no. 14 (2004): 1451–1462, https://doi.org/10.1016/j.ijmachtools.2004.05.008.

12. B. Denkena, H. Liu, F. Pape, et al., "Simulation of Local Contact Conditions in the Secondary Shear Zone in Dry and Wet Metal Cutting," *Procedia CIRP* 117 (2023): 293–298. 19th CIRP Conference on Modeling of Machining Operations, https://doi.org/10.1016/j.procir.2023.03.050.

13. M. Afrasiabi, M. Roethlin, H. Klippel, and K. Wegener, "Meshfree Simulation of Metal Cutting: An Updated Lagrangian Approach With Dynamic Refinement," *International Journal of Mechanical Sciences* 160 (2019): 451–466, https://doi.org/10.1016/j.ijmecsci.2019.06.045.

14. J. Limido, C. Espinosa, M. Salauen, and J. L. Lacome, "Sph Method Applied to High Speed Cutting Modelling," *International Journal of Mechanical Sciences* 49, no. 7 (2007): 898–908, https://doi.org/10.1016/j.ijmecsci.2006.11.005.

15. M. Dehghani, A. Shafiei, and M. M. Abootorabi, "Analyzing Orthogonal Cutting Process Using SPH Method by Kinematic Cutting Tool," *Comptes Rendus. Mécanique* 348, no. 2 (2020): 149–174, https://doi.org/10.5802/crmeca.6.

16. E. Uhlmann, E. Barth, T. Seifarth, M. Höchel, J. Kuhnert, and A. Eisenträger, "Simulation of Metal Cutting With Cutting Fluid Using the Finite-Pointset-Method," *Procedia CIRP* 101 (2021): 98–101, https://doi.org/10.1016/j.procir.2021.02.013.

17. P. Arrazola, T. Özel, D. Umbrello, M. Davies, and I. Jawahir, "Recent Advances in Modelling of Metal Machining Processes," *CIRP Annals* 62, no. 2 (2013): 695–718, https://doi.org/10.1016/j.cirp.2013.05.006.

18. W. Grzesik and J. Rech, "Influence of Machining Conditions on Friction in Metal Cutting Process-A Review," *Mechanik* 4 (2019): 242–248, https://doi.org/10.17814/mechanik.2019.4.33.

19. N. Zorev, "Inter-Relationship Between Shear Processes Occurring Along Tool Face and Shear Plane in Metal Cutting," in *International Research in Production Engineering* (ASME, 1963).

20. B. Peng, T. Bergs, D. Schraknepper, T. Smigielski, and F. Klocke, "Development and Validation of a New Friction Model for Cutting Processes," *International Journal of Advanced Manufacturing Technology* 107, no. 11–12 (2020): 4357–4369, https://doi.org/10.1007/s00170-019-04709-8.

21. C. Bonnet, F. Valiorgue, J. Rech, et al., "Identification of a Friction Model–Application to the Context of Dry Cutting of an AISI 316L Austenitic Stainless Steel With a TiN Coated Carbide Tool," *International Journal of Machine Tools and Manufacture* 48, no. 11 (2008): 1211–1223, https://doi.org/10.1016/j.ijmachtools.2008.03.011.

22. J. Saelzer, S. Berger, I. Iovkov, A. Zabel, and D. Biermann, "Modelling of the Friction in the Chip Formation Zone Depending on the Rake Face Topography," *Wear* 477 (2021): 203802, https://doi.org/10.1016/j.wear.2021.203802.

23. A. Vakis, V. Yastrebov, J. Scheibert, et al., "Modeling and Simulation in Tribology Across Scales: An Overview," *Tribology International* 125 (2018): 169–199, https://doi.org/10.1016/j.triboint.2018.02.005.

24. E. Burman, M. A. Fernández, and S. Frei, "A Nitsche-Based Formulation for Fluid-Structure Interactions With Contact. *ESAIM*," *Mathematical Modelling and Numerical Analysis* 54, no. 2 (2020): 531–564, https://doi.org/10.1051/m2an/2019072.

25. E. Burman, M. A. Fernández, S. Frei, and F. M. Gerosa, "A Mechanically Consistent Model for Fluid-Structure Interactions With Contact Including Seepage," *Computer Methods in Applied Mechanics and Engineering* 392 (2022): 114637, https://doi.org/10.1016/j.cma.2022.114637.

26. C. Ager, B. Schott, A. Vuong, A. Popp, and W. A. Wall, "A Consistent Approach for Fluid-Structure-Contact Interaction Based on a Porous Flow Model for Rough Surface Contact," *International Journal for Numerical Methods in Engineering* 119, no. 13 (2019): 1345–1378, https://doi.org/10.1002/nme.6094.

27. C. Ager, A. Seitz, and W. A. Wall, "A Consistent and Versatile Computational Approach for General Fluid-Structure-Contact Interaction Problems," *International Journal for Numerical Methods in Engineering* 122, no. 19 (2020): 5279–5312, https://doi.org/10.1002/nme.6556.

28. C. Wang, P. Sun, Y. Zhang, J. Xu, Y. Chen, and J. Han, "A Unified-Field Monolithic Fictitious Domain-Finite Element Method for Fluid-Structure-Contact Interactions and Applications to Deterministic Lateral Displacement Problems," *Journal of Computational Physics* 510 (2024): 113083, https://doi.org/10.1016/j.jcp.2024.113083.

29. X. Mao, B. Rath, and R. Jaiman, "A 3d Phase-Field Based Eulerian Variational Framework for Multiphase Fluid-Structure Interaction With Contact Dynamics," *Computer Methods in Applied Mechanics and Engineering* 429 (2024): 117172, https://doi.org/10.1016/j.cma.2024.117172.

30. D. Hilger, N. Hosters, F. Key, S. Elgeti, and M. Behr, "A Novel Approach to Fluid-Structure Interaction Simulations Involving Large Translation and Contact," in *Isogeometric Analysis and Applications 2018* (Springer International Publishing, 2020), 39–56, https://doi.org/10.1007/978-3-030-49836-83.

31. O. Yakhlef and C. M. Murea, "Numerical Simulation of Dynamic Fluid-Structure Interaction With Elastic Structure-Rigid Obstacle Contact," *Fluids* 6, no. 2 (2021): 51, https://doi.org/10.3390/fluids6020051.

32. F. M. Gerosa and A. L. Marsden, "A Mechanically Consistent Unified Formulation for Fluid-Porous-Structure-Contact Interaction," *Computer Methods in Applied Mechanics and Engineering* 425 (2024): 116942, https://doi.org/10.1016/j.cma.2024.116942.

33. H. K. Tönshoff, *Werkzeuge für die moderne fertigung* (Expert Verlag, 1993).

34. A. Gregorio, T. Santos, R. Rossi, A. Jesus, J. Outeiro, and P. Rosa, "Tribology of Metal Cutting: Newly Formed Underside of Chip," *Procedia CIRP* 82 (2019): 136–141, https://doi.org/10.1016/j.procir.2019.04.034.

35. R. Anderson, J. Andrej, A. Barker, et al., "MFEM: A Modular Finite Element Methods Library," *Computers & Mathematics with Applications* 81 (2021): 42–74, https://doi.org/10.1016/j.camwa.2020.06.009.

36. J. A. Cottrell, T. J. R. Hughes, and Y. Bazilevs, *Isogeometric Analysis: Toward Integration of CAD and FEA* (Wiley. OCLC, 2009), ocn335682757.

37. J. Chung and G. M. Hulbert, "A Time Integration Algorithm for Structural Dynamics With Improved Numerical Dissipation: The Generalized-Method," *Journal of Applied Mechanics* 60, no. 2 (1993): 371–375, https://doi.org/10.1115/1.2900803.

38. J. Simo and T. Hughes, *Computational Inelasticity* (Springer, 2006).

39. J. Donea and A. Huerta, *Finite Element Methods for Flow Problems*, 1st ed. (Wiley, 2003), https://doi.org/10.1002/0470013826.

40. A. Johnson and T. Tezduyar, "Mesh Update Strategies in Parallel Finite Element Computations of Flow Problems With Moving Boundaries and Interfaces," *Computer Methods in Applied Mechanics and Engineering* 119, no. 1–2 (1994): 73–94, https://doi.org/10.1016/0045-7825(94)00077-8.

41. T. Spenke, N. Hosters, and M. Behr, "A Multi-Vector Interface Quasi-Newton Method With Linear Complexity for Partitioned Fluid-Structure Interaction," *Computer Methods in Applied Mechanics and Engineering* 361 (2020): 112810. arXiv:2001.07947 [cs], https://doi.org/10.1016/j.cma.2019.112810.

42. T. Spenke, M. Make, and N. Hosters, "A Robin-Neumann Scheme With Quasi-Newton Acceleration for Partitioned Fluid-Structure Interaction," *International Journal for Numerical Methods in Engineering* 124, no. 4 (2023): 979–997, https://doi.org/10.1002/nme.7151.

43. U. Küttler and W. A. Wall, "Fixed-Point Fluid-Structure Interaction Solvers With Dynamic Relaxation," *Computational Mechanics* 43, no. 1 (2008): 61–72, https://doi.org/10.1007/s00466-008-0255-5.

44. N. Hosters, J. Helmig, A. Stavrev, M. Behr, and S. Elgeti, "Fluid-Structure Interaction With NURBS-Based Coupling," *Computer Methods in Applied Mechanics and Engineering* 332 (2018): 520–539, https://doi.org/10.1016/j.cma.2018.01.003.

45. U. Küttler, C. Förster, and W. A. Wall, "A Solution for the Incompressibility Dilemma in Partitioned Fluid-Structure Interaction With Pure Dirichlet Fluid Domains," *Computational Mechanics* 38, no. 4–5 (2006): 417–429, https://doi.org/10.1007/s00466-006-0066-5.

46. M. Make, T. Spenke, N. Hosters, and M. Behr, "Spline-Based Space-Time Finite Element Approach for Fluid-Structure Interaction Problems With a Focus on Fully Enclosed Domains," *Computers & Mathematics with Applications* 114 (2022): 210–224, https://doi.org/10.1016/j.camwa.2022.03.035.

47. A. Beckert, "Coupling Fluid (CFD) and Structural (FE) Models Using Finite Interpolation Elements," *Aerospace Science and Technology* 4, no. 1 (2000): 13–22, https://doi.org/10.1016/S1270-9638(00)00111-5.

48. P. Wriggers, *Computational Contact Mechanics* (Springer, 2006), https://books.google.at/books?id=oBMBy4eMYsQC.

49. F. F. Temizer, P. Wriggers, and T. Hughes, "Contact Treatment in Isogeometric Analysis With NURBS," *Computer Methods in Applied Mechanics and Engineering* 200, no. 9–12 (2011): 1100–1112, https://doi.org/10.1016/j.cma.2010.11.020.

50. L. De Lorenzis, F. F. Temizer, P. Wriggers, and G. Zavarise, "A Large Deformation Frictional Contact Formulation Using NURBS-Based Isogeometric Analysis: APPLICATION OF NURBS-BASED ISOGEOMETRIC ANALYSIS," *International Journal for Numerical Methods in Engineering* 87, no. 13 (2011): 1278–1300, https://doi.org/10.1002/nme.3159.

51. J. Nocedal and S. J. Wright, *Numerical Optimization*, 2nd ed. (Springer. OCLC, 2006), ocm68629100.

52. D. Kraft, *A Software Package for Sequential Quadratic Programming* (DFVLR, 1988).

53. J. Saelzer, Y. Alammari, A. Zabel, D. Biermann, J. Lee, and S. Elgeti, "Characterisation and Modelling of Friction Depending on the Tool Topography and the Intermediate Medium," *Procedia CIRP* 102 (2021): 435–440, https://doi.org/10.1016/j.procir.2021.09.074.

54. L. A. Piegl and W. Tiller, *The NURBS Book*, 2nd ed. (Springer, 1997).

55. G. Johnson and W. Cook, "A Constitutive Model and Data for Metals Subjected to Large Strains, High Strain Rates and High Temperatures," in *Proceedings of the Seventh International Symposium on Ballistics, The Hague, The Netherlands*, vol. 21 (American Defense Preparedness Association, 1983), 541–548.

56. C. E. Rasmussen and C. K. I. Williams, *Gaussian Processes for Machine Learning* (MIT Press, 2005), https://doi.org/10.7551/mitpress/3206.001.0001.

57. F. Pedregosa, G. Varoquaux, A. Gramfort, et al., "Scikit-Learn: Machine Learning in Python," *Journal of Machine Learning Research* 12 (2011): 2825–2830.

58. F. T. Tracy, "Testing Line Search Techniques for Finite Element Discretizations for Unsaturated Flow," in *Computational Science-ICCS 2009*, ed. G. Allen, J. Nabrzyski, E. Seidel, G. D. van Albada, J. Dongarra, and P. M. A. Sloot (Springer Berlin Heidelberg, 2009), 473–480.

59. A. Malakizadi, K. Hosseinkhani, E. Mariano, E. Ng, A. Del Prete, and L. Nyborg, "Influence of Friction Models on Fe Simulation Results of Orthogonal Cutting Process," *International Journal of Advanced Manufacturing Technology* 88, no. 9–12 (2016): 3217–3232, https://doi.org/10.1007/s00170-016-9023-4.

60. R. Sevilla, S. Fernández-Méndez, and A. Huerta, "Nurbs-Enhanced Finite Element Method (Nefem): A Seamless Bridge Between Cad and Fem," *Archives of Computational Methods in Engineering* 18, no. 4 (2011): 441–484, https://doi.org/10.1007/s11831-011-9066-5.